International Journal of Mechanical, Industrial and Aerospace Sciences
ISSN: 2517-9950
Vol:11, No:5, 2017

Development of an Implicit Physical Influence Upwind Scheme for Cell-Centered Finite Volume Method

Shidvash Vakilipour, Masoud Mohammadi, Rouzbeh Riazi, Scott Ormiston, Kimia Amiri, Sahar Barati

***Abstract*—**An essential component of a finite volume method (FVM) is the advection scheme that estimates values on the cell faces based on the calculated values on the nodes or cell centers. The most widely used advection schemes are upwind schemes. These schemes have been developed in FVM on different kinds of structured and unstructured grids. In this research, the physical influence scheme (PIS) is developed for a cell-centered FVM that uses an implicit coupled solver. Results are compared with the exponential differencing scheme (EDS) and the skew upwind differencing scheme (SUDS). Accuracy of these schemes is evaluated for a lid-driven cavity flow at Re = 1000, 3200, and 5000 and a backward-facing step flow at Re = 800. Simulations show considerable differences between the results of EDS scheme with benchmarks, especially for the lid-driven cavity flow at high Reynolds numbers. These differences occur due to false diffusion. Comparing SUDS and PIS schemes shows relatively close results for the backward-facing step flow and different results in lid-driven cavity flow. The poor results of SUDS in the lid-driven cavity flow can be related to its lack of sensitivity to the pressure difference between cell face and upwind points, which is critical for the prediction of such vortex dominant flows.

***Keywords*—**Cell-centered finite volume method, physical influence scheme, exponential differencing scheme, skew upwind differencing scheme, false diffusion.

I. Introduction

IN recent decades, the numerical solution of Navier-Stokes equations using a FVM has been widely developed and improved. In the FVM development, considerable efforts were aimed to properly approximate and linearize the advection terms in the momentum equations. Improper estimation of momentum fluxes crossing cell faces leads to instability or even divergence issues for the numerical solution. In order to preserve stability, upwind schemes have been shown to be appropriate for face value approximations, especially, at high Reynolds numbers.

Shidvash Vakilipour is with the Department of Aerospace Engineering, Faculty of New Sciences and Technologies, University of Tehran, Tehran, Iran (phone: 989121326951, e-mail: vakilipour@ut.ac.ir).

Masoud Mohammadi, Rouzbeh Riazi is with the Department of Aerospace Engineering, Faculty of New Sciences and Technologies, University of Tehran, Tehran, Iran (e-mail: mas.mohammadi@ut.ac.ir, ro_riazi@ut.ac.ir).

Scott Ormiston is with the Department of Mechanical Engineering, University of Manitoba, Manitoba, Canada R3T 5V6, (e-mail: scott.ormiston@umanitoba.ca).

Kimia Amiri is with the Department of Chemical Engineering, University of Amirkabir, Tehran, Iran (e-mail: kimkimamiri@gmail.com).

Sahar Barati is with the Islamic Azadi University, Tehran, Iran (e-mail: saharbarati29@gmail.com).

A most simple upwind scheme is the first order upwind approximation in which the magnitudes of the velocity components on the faces are considered to be equal to their values at neighboring cell center [1]. The upwind neighbor cell is determined based on the flow direction. The first order upwind approximation suffers from numerical false diffusion, and its accuracy deteriorates at low Peclet (Pe) numbers.

To overcome these problems, Spalding [2] proposed the EDS based on one-dimensional solution of the convection-diffusion equation. In this scheme, the velocity magnitude approximation is carried out based on an exponential function of Pe number which requires high computational costs. Furthermore, the numerical results obtained by EDS developed in two and three dimensions are not as accurate as those of one dimensional form. For this reason, a hybrid method was introduced to approximate the EDS by a central difference in $|Pe|<2$ and upwind estimation in $|Pe|>2$ [2]. However, the hybrid method encountered problems such as difference with benchmark solution in $|Pe|\approx2$ and the diffusion term being zero for $|Pe|>2$. For this reason, Patankar and Spalding [3] proposed the power-law scheme in which a fifth order function based on Peclet number is used to estimate face velocities. Although this scheme is more complicated than the hybrid scheme, it offers higher order of accuracy and lower computational costs. In this regard, Raithby and Torrance [4] and Raithby et al. [5] proposed cubic algebraic function and second-order fractional function, respectively that require even lower computational costs with respect to the hybrid and power-law schemes. Furthermore, high order methods such as Quadratic Upwind Interpolation for Convective Kinetics (QUICK) [6], Cubic Upwind Interpolation (CUI), and their modifications [7]-[9] have been developed to reduce the false diffusion.

Although, EDS and its approximations have considerably reduced the numerical false diffusion of upwind schemes, it still produces errors in relatively coarse grids. Those errors increase, particularly, when the flow streamlines are skewed compared to the computational grid lines. Raithby [10], [11] introduced the SUDS considering the upwind direction according to the velocity vector on the cell face. Although SUDS reduces the numerical false diffusion significantly, it encounters numerical dispersion within high gradient regions. Various techniques have been proposed to improve SUDS. Patel et al. [12], [13] utilized flow angles at the corners of control volumes instead of cell faces. They concluded that their scheme performed as well as or better than any of the

existing schemes and it was particularly effective at reducing false diffusion. Van Doormaal et al. [14] included a physical advection correction term which plays the role of interactions between advection, diffusion, and source terms. They showed their scheme introduces only small overshoots and convergence with grid refinement and is more accurate than hybrid schemes. Busnaina et al. [15] proposed a modified type of SUDS, called SUWDS, in which instead of one point in the upwind direction, two points and their weighted average are used.

In order to improve stability and applicability, the MAss-Weighted (MAW) advection scheme was developed in first order [16]-[18] and second order forms [19] for Control Volume Finite Element Methods (CVFEM). In the MAW advection scheme, the face values are weighted by the mass flow ratio crossing that cell face.

Considering the idea of SUDS, Schneider and Raw [20] developed the PIS based on the momentum transport along a streamwise direction between the integration and upwind points. The main idea of the PIS is to consider pressure change and viscous diffusion along the upwind direction. They introduced and implemented the PIS scheme on CVFEM and obtained more acceptable results compared to SUDS. Darbandi and Vakilipour [21] developed this method for unstructured triangular grids and unsteady flow calculations. They also showed the capabilities of the PIS in solving open boundary problems by implementing it on hybrid elements in backward-facing step flow field [22]. Alisadeghi and Karimian [23] also exploited this method for examining the precision and convergence of different face velocity modeling methods and their effects on pressure-velocity field coupling.

The PIS has been successfully developed and implemented on CVFEM's. In the present study, an implicit PIS is developed for a cell-centered FVM. In order to evaluate the accuracy and performance of current developed upwind scheme, the incompressible flow field within Lid-Driven Cavity (LDC) and Backward Facing Step (BFS) are numerically solved using EDS, SUDS, and PIS approaches for the advection scheme. The velocity-pressure fields coupling is established by a Pressure Weighted Interpolation Method (PWIM) and the algebraic linear systems of equations are solved in a coupled manner. The numerical results of the three advection schemes are compared with each other and with benchmark solutions.

II. The Governing Equations

The integral form of the governing equations for incompressible flow without source terms in a stationary grid is as follows:

Continuity equation:

$$\frac{d}{dt}\int_{\Omega}\rho d\Omega+\int_{S}\rho\vec{\boldsymbol{V}}\cdot\mathbf{n}dS=0 \quad (1)$$

X-momentum equation:

$$\frac{d}{dt}\int_{\Omega}\rho U d\Omega+\int_{S}\rho U\vec{\boldsymbol{V}}\cdot\mathbf{n}dS=-\int_{\Omega}\frac{\partial p}{\partial x}d\Omega+\int_{S}\mu\boldsymbol{\nabla}U\cdot\mathbf{n}dS \quad (2)$$

Y-momentum equation:

$$\frac{d}{dt}\int_{\Omega}\rho V d\Omega+\int_{S}\rho V\vec{\boldsymbol{V}}\cdot\mathbf{n}dS=-\int_{\Omega}\frac{\partial p}{\partial y}d\Omega+\int_{S}\mu\boldsymbol{\nabla}V\cdot\mathbf{n}dS \quad (3)$$

where ρ is the fluid density, $\vec{\boldsymbol{V}}$ is the velocity vector, U and V are velocities in x and y directions, respectively, p is the static pressure, and μ is the fluid dynamic viscosity. Also, $\mathbf{n}$, S and Ω denote the control volume face normal vector, face area, and volume, respectively.

III. Computational Modelling

In this research, the computational flow field is discretized by quadrilateral control volumes (cells) using a co-located grid arrangement. The main field variables are stored at the cell centers. Face values are determined at on integration point per face. Fig. 1 shows the numbering and nomenclature of the field cells.

In order to couple the pressure and velocity fields, the continuity equation is discretized using a PWIM similar to the approach of Rhie and Chow [24]. Vakilipour and Ormiston [25] developed a pressure-based finite volume coupled solver using the PWIM for a cell-centered arrangement. The face velocities are estimated by a weighted interpolation of two neighboring cells' momentum equations [25].

For the momentum equations, a first order backward Euler estimation is used to discretize the temporal term. The convection term in the x-Momentum equation is integrated and discretized as follows:

$$\int_{S}\rho U\vec{\boldsymbol{V}}\cdot\mathbf{n}dS=\dot{m}_{e}U_{e}-\dot{m}_{w}U_{w}+\dot{m}_{n}U_{n}-\dot{m}_{s}U_{s} \quad (4)$$

where $\dot{m}_{f=e,w,n,s}$ is the mass flux through the cell faces, and $U_{f=e,w,n,s}$ are the advected velocities.

The pressure terms are approximated as the average of pressure gradient in the cell volume:

$$-\int_{\Omega}\frac{\partial p}{\partial x}d\Omega=-\Omega_{P}\left.\frac{\partial p}{\partial x}\right|_{P} \quad (5)$$

The viscous terms are rewritten as the viscous flux normal to the face:

$$\int_{S}\mu\boldsymbol{\nabla}U\cdot\mathbf{n}dS=\mu\int_{S}\left(\frac{\partial U}{\partial n}\right)dS=\sum_{f=e,w,n,s}\left(\mu S_{f}\left.\frac{\partial U}{\partial n}\right|_{f}\right) \quad (6)$$

The derivatives normal to the faces are written in terms of unit vectors $\hat{n}$, $\hat{s}$ and $\hat{t}$:

$$\left.\frac{\partial U}{\partial n}\right|_{e}=\frac{1}{\hat{n}_{e}\cdot\hat{s}_{e}}\left(\left.\frac{\partial U}{\partial s}\right|_{e}-\left.\frac{\partial U}{\partial t}\right|_{e}\hat{t}_{e}\cdot\hat{s}_{e}\right) \quad (7)$$

$$\left.\frac{\partial U}{\partial n}\right|_{n}=\frac{1}{\hat{n}_{n}\cdot\hat{t}_{n}}\left(\left.\frac{\partial U}{\partial t}\right|_{n}-\left.\frac{\partial U}{\partial s}\right|_{n}\hat{t}_{n}\cdot\hat{s}_{n}\right) \quad (8)$$

The normal derivative of the U-velocity on the east cell face is divided into a component from east to west, $\partial U/\partial s|_{e}$, and one from south to north, $\partial U/\partial t|_{e}\hat{t}_{e}\cdot\hat{s}_{e}$. The velocity

derivatives in *s* and *t* directions are approximated using a central difference method.

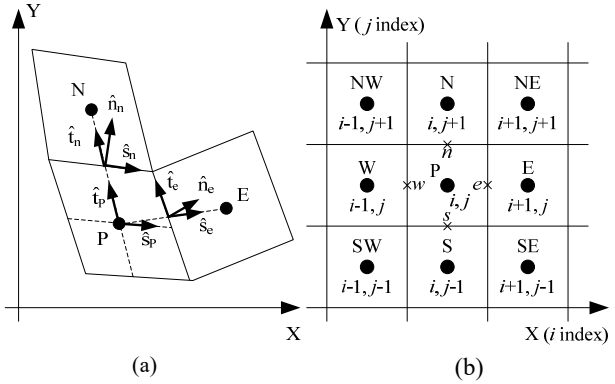

Fig. 1 Right: nomenclature for cell faces of the cell *P* and its neighboring control volumes, Left: co-located variable storage

A. Approximation of the Momentum Advection Fluxes

Among the advection, diffusion and pressure terms, the advection terms often have the most influence on the solution and are the most difficult to estimate. Here, the relations used for the EDS, the SUDS, and the PIS are now presented. Their behavior will be discussed in Section IV.

1) Exponential Differencing Scheme (EDS)

To approximate the advected velocities of the momentum equations on the cell faces by EDS, the approach presented by Raithby and Schneider [26] is used. For example, the U-velocity on the cell east face is estimated by:

$$U_e = (0.5 + \alpha_e)U_P + (0.5 - \alpha_e)U_E \tag{9}$$

where α_e is defined as follows:

$$\alpha_e = sign(\dot{m}_e)\frac{0.5Pe_e^2}{5+Pe_e^2} \tag{10}$$

In (10), *Pe* is the cell Peclet number, which is defined as:

$$Pe_e = \frac{\rho U_e (ds)_e}{\mu} \tag{11}$$

where $(ds)_e$ is the distance between the *P* and E nodes.

2) Skew Upwind Differencing Scheme (SUDS)

Referring to Fig. 2, another way of presenting an estimated value for the variable ϕ on the cell face f, for example, is [10], [15], [18]:

$$\phi_f = \phi_{\text{up}} + \Delta\phi_f \tag{12}$$

where $\Delta\phi_f$ represents the variation of ϕ_f from the upstream (up) to the integration point location. In the SUDS, it is assumed that $\Delta\phi_f = 0$, and therefore $\phi_f = \phi_{\text{up}}$. In Fig. 2, locating of upwind point is shown for the east face of cell P in the cell-centered control volume arrangement. As seen in this figure, a line is considered upstream along the velocity vector direction at the integration point *e* on the east face. This line intersects one of the straight lines connecting cell centers around point *e* at upstream point *up*. The distance between the points *e* and *up* is named the upwind length, L_{up}. The velocity at upstream point, u_{up}, is calculated using a weighted average of velocities of two cell centers at the ends of intersected line.

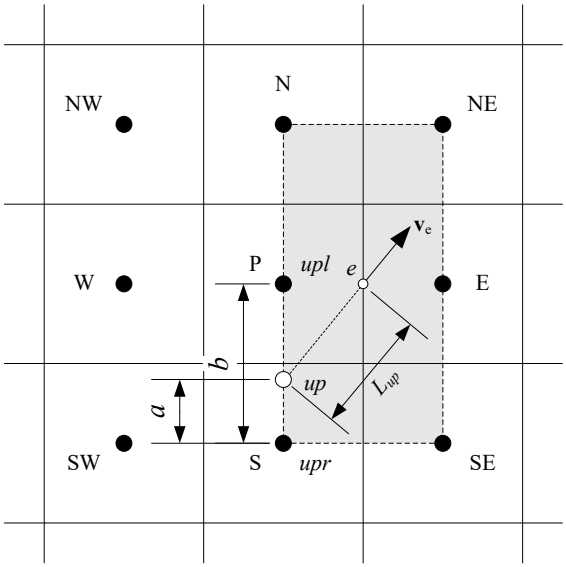

Fig. 2 An element constructed from cell centers surrounding the point *e* of cell *P*, and representation of the skew upwind point for point *e*; here, cell centers *S* and *P* are the right (upr) and left (upl) points of the upwind point (*up*), respectively

$$\left(u_{up}\right)_e = \left[\frac{a}{b}U_{upr} + \left(1 - \frac{a}{b}\right)U_{upl}\right]_e \tag{13}$$

In (13), subscripts *upr* and *upl* indicate the left and right cell centers with respect to the upwind point *up*. Also, *a* and *b* are the distances between points *up* and *upr* and the length of intersected line, respectively. In Fig. 2, the upwind point *up* is predicted to be on the line connecting cell centers *S* and *P*. In this regard, point *S* represents *upr* and *P* represents *upl*. The SUDS scheme is stablished by substitution of face velocity U_e with u_{up}.

3) Physical Influence Scheme (PIS)

In the SUDS, a linear approximation is established between face and its streamwise upwind points. In PIS, however, the linear momentum equations are used to generate a comprehensive approximation for $\Delta\phi_f$ in (12) [19]:

$$\rho\frac{\partial u}{\partial t} + \rho V_{tot}\frac{\partial u}{\partial s} - \mu\nabla^2 u + \frac{dp}{dx} = S_{diff}^x \tag{14}$$

$$\rho\frac{\partial v}{\partial t} + \rho V_{tot}\frac{\partial v}{\partial s} - \mu\nabla^2 v + \frac{dp}{dy} = S_{diff}^y \tag{15}$$

where $V_{tot} = (\overline{U}_e^2 + \overline{V}_e^2)^{1/2}$, and *s* represents the flow direction. $\overline{U}_e$ and $\overline{V}_e$ are the velocity components on the face point *e*, and their values are computed from the last iteration.

S_{diff}^{x} and S_{diff}^{y} are treated as source terms and taken to their right-hand side. Equations (13) and (14) are used to approximate U and V on the cell faces. Considering the upwind direction, the $\partial u/\partial s$ term could be discretized using a backward difference:

$$\left(\rho V_{tot}\frac{\partial u}{\partial s}\right)_e \approx \left(\rho V_{tot}\frac{U-U_{up}}{L_{up}}\right)_e \quad (16)$$

where e represents the east face point of the cell P. Finding the upwind point and estimating the value of U_{up} can be done in the same way as in the SUDS. The pressure and diffusion terms in (14) and (15) are discretized using a central difference approximation.

IV. Results and Discussion

The numerical results of the present coupled finite volume solver using the three aforementioned advection schemes are presented in this section. Two steady-flow test cases are studied: a lid-driven cavity and a backward-facing step. Therefore, in spite of the general unsteady form of the current algorithm, time step size of 10^8 seconds is used to achieve the steady state solution of the problems. No relaxation factors are used in the discretized equations.

A. Lid-Driven Cavity (LDC) Flow

The lid-driven cavity flow field including the boundary conditions, grid zones, and the dominant flow structures are shown in Fig. 3. The flow field is a unit length square bounded to stationary walls at bottom, left, and right sides, and a moving wall on top with velocity of u =1 and v = 0. As seen in Fig. 3, the dominant flow structures involve a primary vortex at the center and a number of secondary vortices in the corners. The secondary vortices in the bottom-right, bottom-left, and top-left are labeled BR, BL, and TL, respectively. The Reynolds number of flow within presented square cavity is defined by $Re = \rho/\mu$. The numerical simulations of flow field within square cavity were obtained for Reynolds numbers of 1000, 3200, and 5000 by varying the dynamic viscosity. The numerical results are compared with those of Ghia et al. [27].

1) Computational Grid and Grid Independence of the Solution

To study the characteristics of the secondary vortices, the flow field is divided into nine parts with different grid resolutions (see Fig. 3). The four corner parts and the middle part have a length of L_c = 0.25 and L_m = 0.5, respectively. The number of divisions in corner parts is the same; however, in middle part, it is 1.2 to 1.7 times more than the corners. This field zoning allows for grid refinement in areas containing vortices and results in better capturing of such flow structures.

One of the notable characteristics of the three aforementioned advection schemes is their dependence on the computational grid resolution. Fig. 4 presents the variation of the maximum x velocity (at x=0.5 and y<0.5) and the maximum y velocity (at x<0.5 and y=0.5) with grid resolution Reynolds numbers of 1000 and 3200. The coarse grid for the numerical simulations at Re=1000 and 3200 are 55×55 and 69×69, respectively. The variations with respect to the base grid are calculated by:

$$RD(\%) = 100 \times (\varphi - \varphi_0)/\varphi_0 \quad (17)$$

where φ_0 and φ are the maximum x or y velocities in coarse and fine grids, respectively. Therefore, RD is relative percentage difference between those quantities. As seen in Fig. 4, the relative difference for the EDS is increasing linearly and reaches 60% in the finest grid. These differences are more moderate for the SUDS and reach 20% for the finest grid. However, the rate of difference is far less for the PIS results and is 5% in the finest grid. These results indicate that the PIS demonstrates a significant reduction in sensitivity of numerical solutions to the grid resolution compared to the other two schemes.

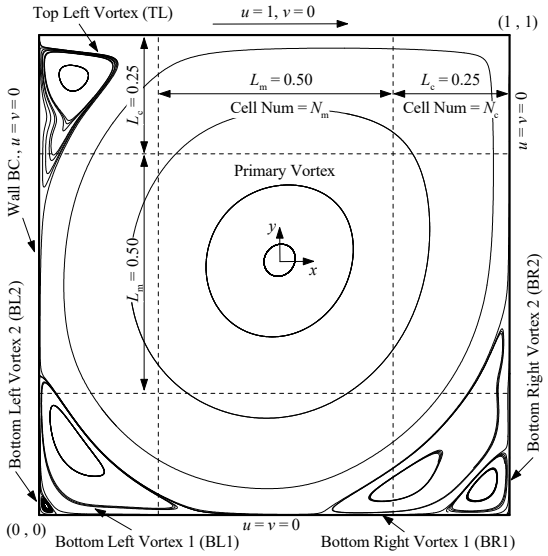

Fig. 3 Lid-driven cavity flow field, boundary conditions, grid zones, and its dominant flow structures

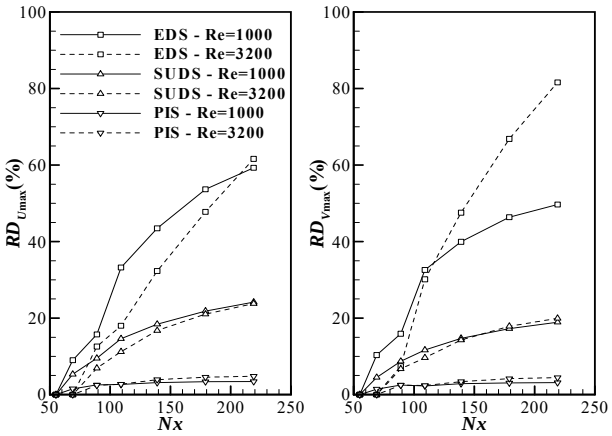

Fig. 4 The grid dependence study in LDC flow according to maximum u and v velocities at mid-sections for Re = 1000 and 3200

2) Velocity Profiles

Fig. 5 shows the horizontal and vertical velocity distributions along middle sections of the cavity for the three Reynolds numbers utilizing the three upwind schemes. The numerical results of the PIS are significantly more accurate than those of the EDS and the SUDS. As mentioned earlier, the EDS suffers from false diffusion in flows in which streamlines are not aligned with gridlines. The LDC flow is an example of such a flow and the effects of false diffusion on the EDS results are clearly observed in Fig. 4, especially at high Reynolds numbers. Although the results of the SUDS are relatively better than those of the EDS, they still deviate from the results given by Ghia et al. [27]. In this case, the first order SUDS is not able to provide adequate accuracy and requires modifications such as higher order approximations or mass weighted average SUDS [15]-[17]. On the other hand, the PIS has been able to estimate precise velocity fields and maintain good performance up to a Reynolds number of 5000.

3) Streamlines and Vortices

In Fig. 6, the streamlines for the LDC flow field are shown for different Reynolds numbers. Of particular interest in the streamline plots are the strength and shape of the secondary vortex structures, especially TL, BL2, and BR2 vortices. Generally, due to significant false diffusion, the EDS predicts smaller corner eddies compared to the SUDS and the PIS. At a Reynolds number of 3200, the TL vortex is not predicted by the EDS, and at a Reynolds number of 5000, the EDS does not resolve the BL2 and BR2 vortices. These vortices are slightly better predicted by the SUDS, but significant differences still remain between the SUDS results and those of the PIS. The PIS is capable of resolving all vortices more precisely. In order to study quantitatively the performance of advection schemes to resolve the vortices, the y coordinates of the centers of resolved vortices are extracted and compared with those of Ghia et al. [27] and illustrated in Fig. 7. The comparisons depicted in Fig. 7 show that the PIS results in more accurate velocity fields which are in excellent agreement with those of the benchmark solution.

B. Backward-Facing Step (BFS) Flow

1) The Flow Field, Boundary Conditions and the Governing Flow Structures

The backward-facing step flow filed, its imposed boundary conditions, grid zones, and the dominant flow structures are shown in Fig. 8. The flow field is a rectangle with the height H and length $30H$ bounded with a stationary wall at the top and bottom sides. The left boundary has a no-slip wall at the bottom half and an inlet velocity with a parabolic U-velocity distribution at the top half. The right side is considered as the outlet section where the fully developed boundary condition is specified. A channel aspect ratio of 30 is considered large enough to expect that fully developed boundary condition could be imposed at the outlet boundary.

The Reynolds number for this flow is defined by $\mathrm{Re} = \rho U_{ave} H/\mu$, where U_{ave} is the average U-velocity at the inlet boundary. The flow Reynolds number is set to 800. Two recirculation zones are formed at the lower left corner and adjacent the upper wall denoted by LW and UW, respectively. The numerical results of the flow simulations over backward facing step are compared with those of Gartling [28].

2) The Computational Grid and Grid Independence of the Solution

To discretize the computational domain, the flow field is divided into two zones in x direction: the first part from x/H=0 to 12 (L_1=12H) and the second part from x/H=12 to 30 (length of L_2=18H). In the first part, longitudinal grid decomposition enables controls on grid resolution in recirculation zones near the inlet boundary and prevents irregular increase in the grid spacing. In this part which contains two recirculating flow structures, three uniform grid spacings of Nx_2 = 120, 180, and 240 are considered for coarse, medium and fine arrangements. The second part of flow field is where the flow reaches the fully developed condition near the outlet section. In this part, the number of divisions is constant (Nx_2 = 60) and the spacing increases gradually from x/H = 12 to x/H = 30 with an expansion ratio of 1.035. The grid spacing along y direction is uniform with Ny = 62, 92, 122, and 152 for the coarse, medium, and fine grid arrangements, respectively.

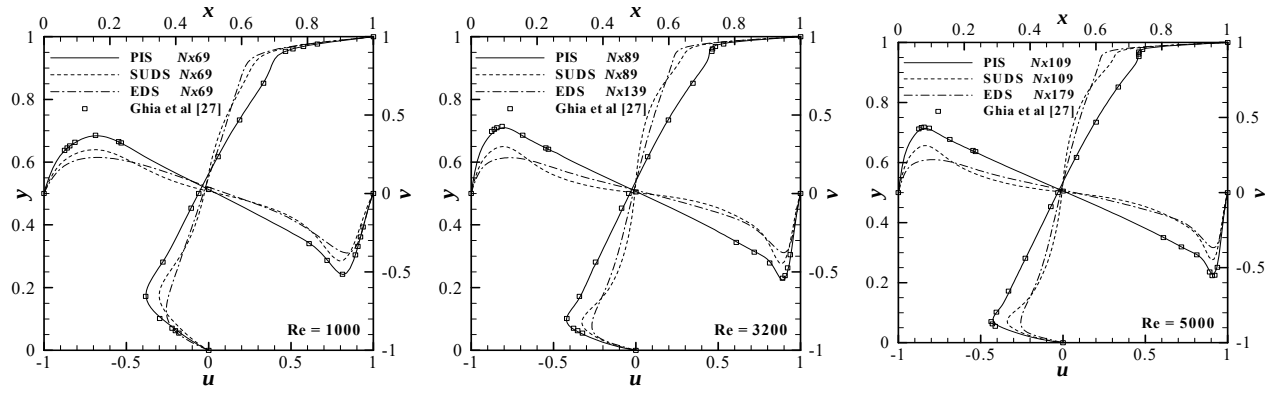

(a) Re = 1000 (b) Re = 3200 (c) Re = 5000

Fig. 5 Velocity profiles in lid-driven cavity flow at mid-sections for various upwind schemes

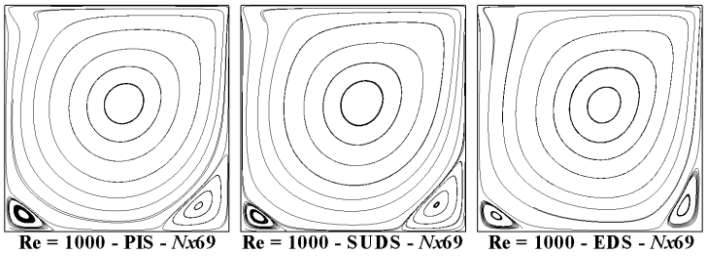

(a) Re = 1000

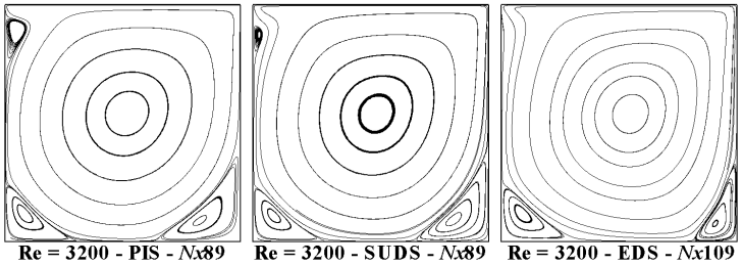

(b) Re = 3200

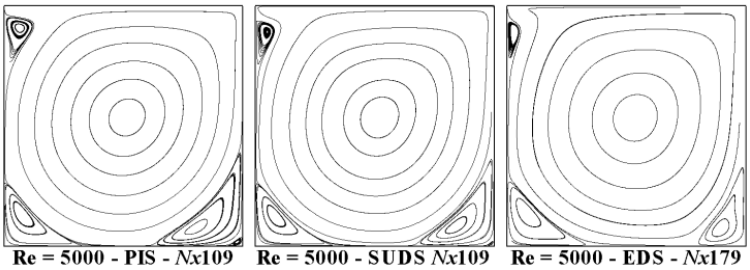

(c) Re = 5000

Fig. 6 Streamlines in lid-driven cavity flow for various upwind schemes at different Reynolds numbers.

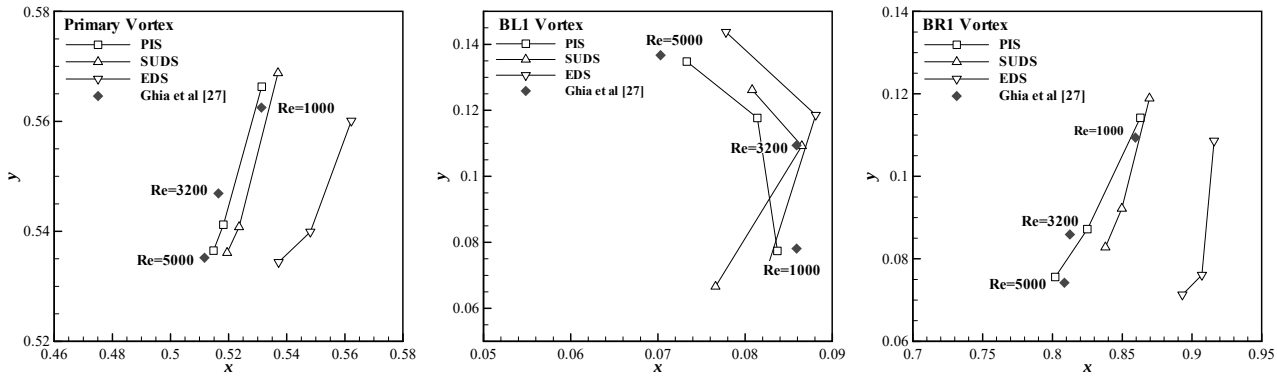

(a) Primary vortex (b) BL1 vortex (c) BR1 vortex

Fig. 7 Coordinates of the center of lid-driven cavity vortices at different Reynolds numbers predicted by the advection schemes

The grid independence of the solution is studied by examining the maximum x and y velocities at $x = 7H$. The results from the PIS are shown in Fig. 9. The relative percentage difference, $RD\%$, with respect to the base grid (180×62) was calculated using (16). As seen in Fig. 9, the sensitivity of the maximum x-velocity to the grid size is less than 0.1% and is negligible. On the other hand, the variation of y-velocity is significant (about 10-50%). Accordingly, the 240×122 grid was finally chosen for flow computations. Note that $Nx = 240$ in this mesh means the sum of 180 cells on L_1 and 60 cells on L_2 (Fig. 8).

3) Velocity and Pressure Profiles

In Fig. 10, the velocity field profiles at two sections, $x = 7H$ and $x = 15H$, and pressure profiles along the bottom and top walls are shown for the three advection schemes. There are notable deviations for the EDS results from those of Gartling [28]. For the x-velocity, u, this deviation is obvious at maximum and minimum velocities, especially at $x = 7H$. The SUDS results are in very good agreement with the results of Gartling. Likewise, the results obtained by the PIS are in excellent agreement with those of Gartling. The differences between the numerical results of EDS and two other upwind schemes are also evident in the pressure profile along bottom and top walls. In addition, the pressure field obtained by PIS is in excellent agreement accordance with those of benchmark [28], especially, at the pressure maximum and minimum points

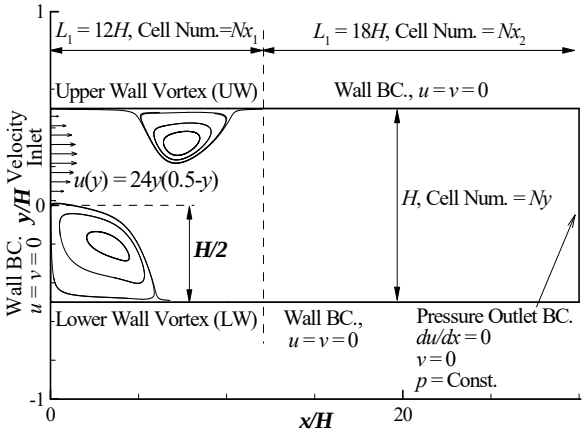

Fig. 8 The BFS flow field, boundary conditions, grid zones, and its dominant flow structures

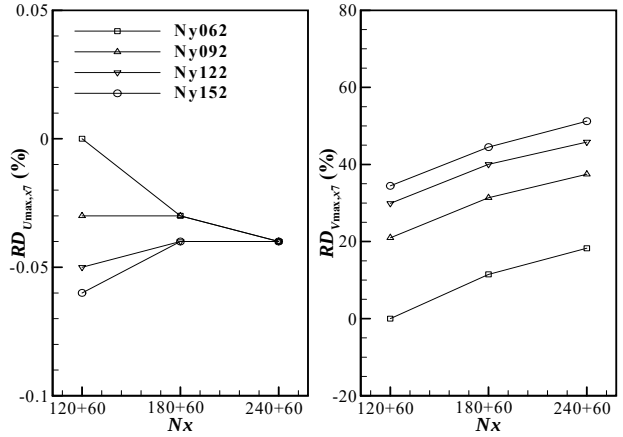

Fig. 9 Grid dependence study for the BFS flow for the PIS scheme using velocities at $x = 7H$

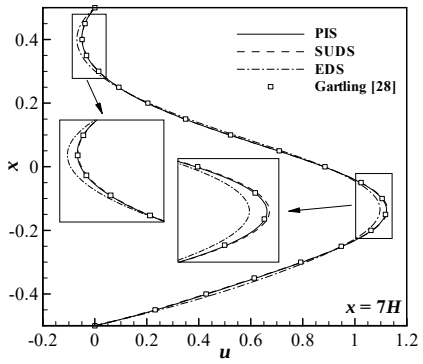

(a) u-velocity at x=7H

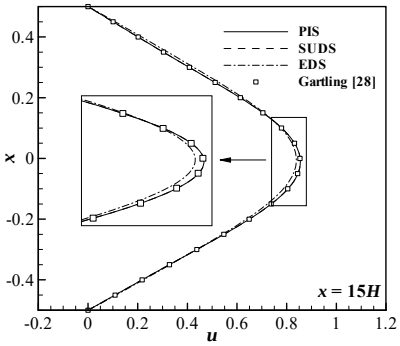

(b) u-velocity at x=15H

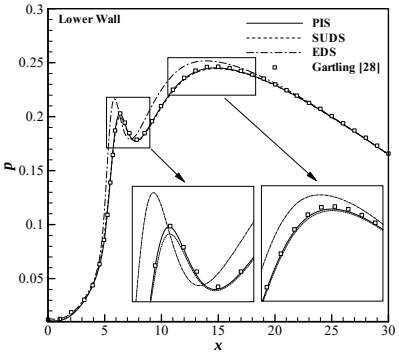

(c) lower wall pressure

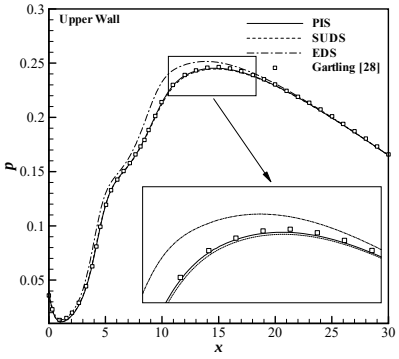

(d) upper wall pressure

Fig. 10 Velocity profiles at $x = 7H$ and $x = 15H$ and pressure profiles on the lower and upper walls for the BFS for three advection schemes

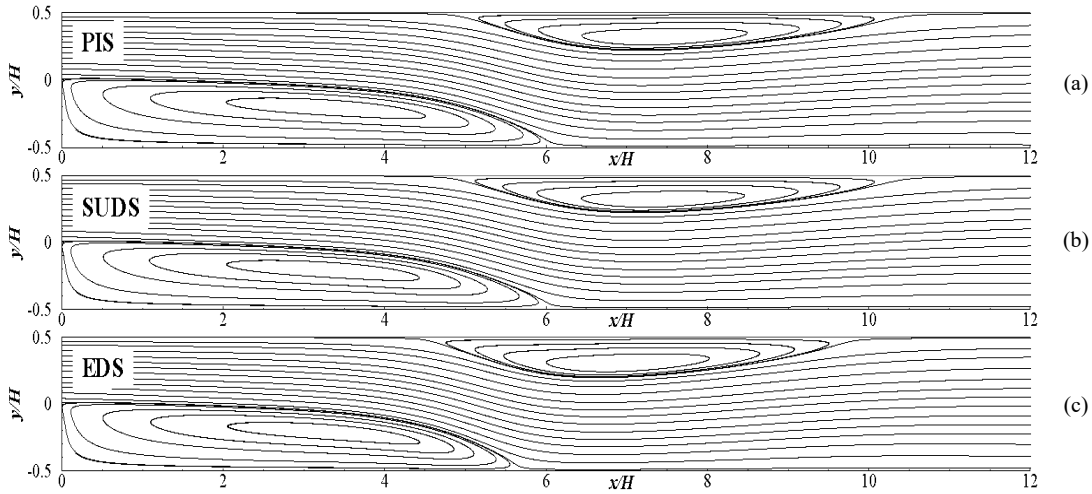

Fig. 11 Streamlines and vortices downstream of the BFS for three advection schemes

TABLE I
THE LENGTH AND COORDINATES OF THE CENTER OF THE LOWER AND UPPER VORTICES IN THE BFS FLOW

Parameter	Gartling [28]	Present Work			Difference with Gartling [28]		
		EDS	SUDS	PIS	EDS	SUDS	PIS
$x_{cen,LW}$	3.350	3.392	3.385	3.385	1.3%	1.0%	1.0%
$y_{cen,LW}$	-0.200	-0.210	-0.205	-0.204	5.1%	2.5%	2.2%
L_{LW}	6.100	5.669	6.070	6.072	-7.1%	-0.5%	-0.5%
$x_{cen,UW}$	7.400	6.981	7.417	7.429	-5.7%	0.2%	0.4%
$y_{cen,LW}$	0.300	0.301	0.316	0.314	0.2%	5.2%	4.8%
L_{UW}	5.630	5.402	5.716	5.648	-4.0%	1.5%	0.3%

4) Streamlines and Vortices

Fig. 11 presents the dominant streamlines and vortices of the BFS flow for the three advection schemes. Qualitatively, it is seen that the locations of the separation and reattachment points predicted by the EDS are upstream of those predicted by the SUDS and the PIS. The results of the SUDS and the PIS show predictions of vortices of similar shape and size. The specifications of bottom and top vortices resolved by the advection schemes are presented in Table I alongside with the Gartling results [28]. The results in Table I show the relatively poor performance of the EDS, especially, in prediction of longitudinal location of the center and size of the vortices. On the other hand, the SUDS and the PIS results are relatively similar for the lower wall vortex (LW). But, the PIS yielded the most accurate results for the upper wall vortex (UW), especially, in estimating the vortex length.

V. CONCLUDING REMARKS

The PIS is evaluated and developed in many Control Volume Finite Element Methods (CVFEM) studies on different structured and unstructured square and triangular grids. This approach was developed in cell-centered control volume method with coupled solver in the present study, and the results were compared with two other common advection schemes: the EDS and the SUDS.

Lid-driven cavity and backward-facing step flows were used to examine the performance of the three advection schemes. These flows intensify both factors of false diffusion in advection schemes: (1) high Reynolds number and (2) misalignment of the streamlines and gridlines (due to the existence of vortices). The lid-driven cavity flow field was solved at one relatively high Reynolds number (1000), and at two high Reynolds numbers (3200 and 5000). The backward-facing step flow was solved at a Reynolds number of 800. The present analysis yielded the following observations (a) the EDS results do not have a good accuracy at high Reynolds numbers for the lid-driven cavity flow; its accuracy was relatively better, but for the backward-facing step flow. The reason is the misalignment between streamlines and gridlines in cavity flow compared to the step flow, (b) the convergence rate with grid size of the EDS is lower than the other two schemes and also more dependent on the grid size; in the lid-driven cavity flow, the EDS does not converge in the same grids as the PIS and the SUDS, (c) examining the flow lines and vortex structures of cavity flow in the EDS results shows that the vortices are much smaller than expected due to the intense false diffusion, and in some cases secondary vortices do not form unless a finer grid is used, (d) comparing the results of the SUDS, the PIS shows them to be close for backward-facing step flow and far apart for the lid-driven cavity flow. The significant difference for the lid-driven cavity flows can be attributed to the lack dependence on the pressure difference between cell face and upwind point; including this extra physics can improve the accuracy of the upwind

approximation. In the lid-driven cavity flow, due to dominant vortex flow, the difference between pressure gradients on cell faces is much greater than in the backward-facing step flow. In the backward-facing step flow, where the pressure gradients are milder, the SUDS results are close to the results obtained by the PIS, (e) The convergence rate of the SUDS and the PIS are very close to each other and their dependency to the grid size are much less than the EDS, and (f) the PIS performed much better in capturing the vertical structures of the flow; this scheme provided the best agreement with reference results because it maintains a strong relation between the advection term and the pressure field and diffusion terms by using a momentum equation along the flow line.

REFERENCES

[1] S. V. Patankar, Numerical Heat Transfer and Fluid Flow. Series in Computational Methods in Mechanics and Thermal Sciences. New York: McGraw-Hill, 1980.
[2] D. B. Spalding, "A novel finite difference formulation for differential expressions involving both first and second derivatives," Int. J. Numer. Method Eng., vol. 4, no. 4, pp. 551-559, 1972.
[3] S. V. Patankar and D.B. Spalding, "A calculation procedure for heat, mass and momentum transfer in three-dimensional parabolic flows," Int. J. Heat Mass Tran., vol. 15, p. 1787, 1972.
[4] G. D. Raithby, K. E. Torrance, "Upstream weighted differencing schemes and their application to elliptic problems involving fluid flow," Comput. Fluids, vol. 8, no.12, pp. 191–206, 1974.
[5] G. D. Raithby, P. F. Galpin, J. P. Van Doormaal, "Prediction of heat and fluid flow in complex geometries using general orthogonal coordinates," Numer. Heat Tr. A-Appl., vol. 9, no. 2, pp. 125-142, 1986.
[6] B. P. Leonard, "A stable and accurate convective modeling procedure based on quadratic upstream interpolation," Comput. Methods Appl. M., vol. 19, no. 1, pp. 59–98, 1979.
[7] T. Han, J. A. C. Humphrey, B. E. Launder, "A comparison of hybrid and quadratic-upstream differencing in high Reynolds number elliptic flows," Comput. Methods Appl. M., vol. 29, no. 1, pp. 81-95, 1981.
[8] Pollard, A. L. W. Siu, "The calculation of some laminar flows using various discretisation schemes," Comput. Methods Appl. M., vol. 35, no. 3, pp. 293-313, 1982.
[9] T. Hayase, J. A. C. Humphrey, R. Greif, "A consistently formulated QUICK scheme for fast and stable convergence using finite-volume iterative calculation procedures," J. Comput. Phys., vol. 98, No. 1, pp. 108-118, 1992.
[10] G. D. Raithby, "A critical evaluation of upstream differencing applied to problems involving fluid flow," Comput. Methods Appl. M., vol. 9, No. 1, pp. 75-103, 1976.
[11] G. D. Raithby, "Skew upstream differencing schemes for problems involving fluid flow," Comput. Methods Appl. M., vol. 9, no. 2, pp. 153-164, 1976.
[12] M. K. Patel, M. Cross, N. C. Markatos, "An assessment of flow oriented schemes for reducing 'false diffusion'," Int. J. Numer. Meth.Eng., vol. 26, no.10, pp.2279-2304, 1988.
[13] M. K. Patel, N. C. Markatos, M. Cross, "Method of reducing false-diffusion errors in convection—diffusion problems," Appl. Math. Model., vol. 9, no. 4, pp. 302-306, 1985.
[14] J. P. Van Doormaal, A. Turan, G. D. Raithby, "Evaluation of new techniques for the calculation of internal recirculating flows," Paper No. AIAA-87-0059, AIAA 25th Aerosp. Sci. Meet., Reno, NV, Jan. 12-15, 1987.
[15] A.A. Busnaina, X. Zheng, M.A.R. Sharif, "A modified skew upwind scheme for fluid flow and heat transfer computations," Appl. Math. Model., vol. 15, No. 8, pp. 425-432, 1991.
[16] G. E. Schneider, M. J. Raw, "A skewed, positive influence coefficient upwinding procedure for control-volume-based finite-element convection-diffusion computation," Numer. Heat Tr. A-Appl., vol. 9, no. 1, pp. 1-26, 1986.
[17] H. J. Saabas, B. R. Baliga, "Co-located equal-order control-volume finite-element method for multidimensional, incompressible, fluid flow—Part II: verification," Numer. Heat Transfer, vol. 26, no. 4, pp. 409-424, 1994.
[18] Masson, C., H. J. Saabas, B. R. Baliga, "Co-located equal-order control-volume finite element method for two-dimensional axisymmetric incompressible fluid flow," Int. J. Numer. Meth. Fl., vol. 18, no. 1, pp. 1-26, 1994.
[19] L. Dung Tran, M. Christian, S. Arezki, "A stable second-order mass-weighted upwind scheme for unstructured meshes," Int. J. Numer. Meth. Fl., vol. 51, no.7, pp.749-771, 2006.
[20] G. E. Schneider, M. J. Raw, "Control volume finite element method for heat transfer and fluid flow using collocated variables. 1. Computational procedure; 2. Application and validation," Numer. Heat Transfer, vol. 11, no. 4, pp. 363–400, 1987.
[21] M. Darbandi, S. Vakilipour, "Developing implicit pressure-weighted upwinding scheme to calculate steady and unsteady flows on unstructured grids," Int. J. Numer. Meth. Fl., vol. 56, no. 2, pp. 115-141, 2008.
[22] M. Darbandi, S. Vakilipour, "Using fully implicit conservative statements to close open boundaries passing through recirculations," Int. J. Numer. Meth. Fl., vol. 53, no.3, pp. 371-389, 2007.
[23] H. Alisadeghi, S. M. H. Karimian, "Different modelings of cell-face velocities and their effects on the pressure–velocity coupling, accuracy and convergence of solution," Int. J. Numer. Meth. Fl., vol. 65, no. 8, pp. 969-988, 2011.
[24] M. Rhie, W. L Chow, "Numerical study of the turbulent flow past an airfoil with trailing edge separation," AIAA J., vol. 21, no. 11, pp. 1525–1532, 1983.
[25] S. Vakilipour, S. J. Ormiston, "A coupled pressure-based co-located finite-volume solution method for natural-convection flows," Numer. Heat Tr. B-Fund., vol. 61, no. 2, pp. 91-115, 2012.
[26] G. D. Raithby and G. E. Schneider, "Elliptic Systems: Finite-Difference Methods II," in Handbook of Numerical Heat Transfer, W. J. Minkowycz, E. M. Sparrow, G.E. Schneider, and R. H. Pletcher (Eds.), New York: Wiley, 1988, pp. 241-292.
[27] U. K. N. G. Ghia, K. N. Ghia, C. T. Shin, "High-Re solutions for incompressible flow using the Navier-Stokes equations and a multigrid method," J. comput. Phys., vol. 48, no. 3, pp. 387-411, 1982.
[28] K. Gartling, "A test problem for outflow boundary conditions—flow over a backward-facing step," Int. J. Numer. Meth. Fl., vol. 11, no. 7, pp. 953-967, 1990.